Accurate Small-Signal Modeling and Stability Analysis of Wide-Input Buck Converter Considering Modulation Waveform Ripples

Xiangpeng Cheng, *Student Member, IEEE*, Jinjun Liu, *Fellow, IEEE*, and Zeng Liu, *Member, IEEE*

***Abstract*—Buck converters are widely used in consumer electronics, electric vehicles, and dc microgrids. Small-signal models are necessary tools to design high-quality controllers. However, most of them neglect modulation waveform ripples, which introduces significant errors under high-bandwidth controls. Recently, two models explain the influences of nondifferentiable modulation waveform ripples by their left-side derivatives at crossing points. However, this conclusion is built on the premise that infinite sideband components caused by switching have been considered, which largely complicates these models. The accurate small-signal model with finite sideband components is proposed for nondifferentiable modulation waveform ripples in this article. Based on it, the stable working region and control design of wide-input high-bandwidth Buck converters are talked about. Simulations and experiments validate the accuracy and effectiveness of the proposed model.**

***Index Terms*—Buck converters, high control bandwidth, modulation waveform ripples (MWRs), small-signal model.**

I. INTRODUCTION

DC/DC converters feature with strong nonlinearity and time variance due to switching effects. The small-signal averaged model transforms them into linear and time-invariant systems to simplify control designs [1]. As shown in Fig. 1, this model is built on the following two basic assumptions from the perspective of the frequency domain [2].

1) The dc component of modulation waveforms (solid line on 0 of the horizontal axis) is treated as pulsewidth modulation (PWM) steady-state operating points, while modulation waveform ripples (MWRs) are ignored (other solid lines on horizontal axis).
2) The output perturbation of PWM merely considers the fundamental frequency component (dashed lines on $\pm\omega_p$ of the horizontal axis), while sideband components caused by switching (other dashed lines) are neglected.

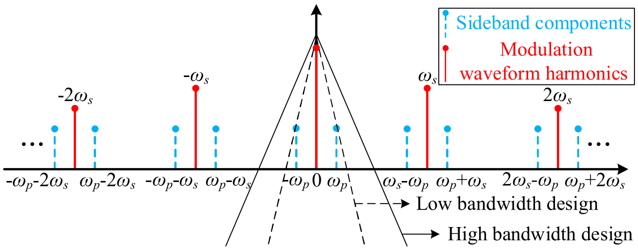

Fig. 1. Modulation waveform harmonics in steady state and sideband components under small-signal perturbation, where ω_s and ω_p represent the switching frequency and the small-signal perturbation frequency in angular form.

Many research articles have shown that enhancing control bandwidth can speed up transient responses and reduce required output capacitors of voltage regulators [3]–[5]. However, the capability of Buck converters to suppress high-frequency components is reduced under high-bandwidth controls, which weakens the accuracy of small-signal averaged model due to its ignorance of MWRs and sideband components.

Wide-input Buck converters will play an important role for the rapid development of automotive technologies, small and medium power satellite systems, renewable energy utilizations, and battery-powered hand-held devices [6]–[8]. The variation of the input voltage will cause the variation of MWRs. The small-signal averaged model without considering MWRs is also invalid for stability judgments and control designs of such systems during the whole working region.

Different approaches have been developed to solve these issues. There are three modeling skills, i.e., numerical models, discrete-time models, and continuous-time models [9]. Numerical models utilize various algorithms to obtain arithmetic solutions of converters' behaviors [10], [11]. Simulators are commonly based on those models to describe systems accurately, but they lack physical meanings to aid control designs. Discrete-time models calculate state-space equations of converters at the beginning or ending of each switching interval and analyze corresponding small-signal models in the z domain [12], [13]. Those models always sacrifice tremendous complexity for accuracy, which is unfriendly to be used in practical designs. Most engineers are more familiar with analytical tools in the s domain, so continuous-time models are most popular.

Manuscript received April 14, 2021; revised August 5, 2021 and October 22, 2021; accepted December 31, 2021. Date of publication January 6, 2022; date of current version February 18, 2022. Recommended for publication by Associate Editor C.-J. Chen. *(Corresponding authors: Jinjun Liu; Zeng Liu.)*

The authors are with the State Key Laboratory of Electrical Insulation and Power Equipment, School of Electrical Engineering, Xi'an Jiaotong University, Xi'an 710049, China (e-mail: alexcheng1994@163.com; jjliu@mail.xjtu.edu.cn; zengliu@mail.xjtu.edu.cn).

Color versions of one or more figures in this article are available at https://doi.org/10.1109/TPEL.2022.3140851.

Digital Object Identifier 10.1109/TPEL.2022.3140851

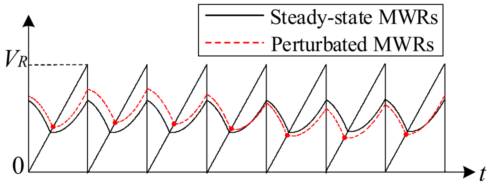

Fig. 2. Perturbated MWRs from closed-loop view.

Recently, many analytical models take sideband components into consideration. The multifrequency small-signal model incorporates one dominant sideband component $\omega_p - \omega_s$ [14], while the matrix-based small-signal model adds another two sideband components $\omega_p + \omega_s$ and $\omega_p - 2\omega_s$ [15]. Although they can predict the magnitude attenuation and phase delay of loop gains around switching frequency, the ignorance of MWRs limits their accuracy.

According to the mathematical characteristics of MWRs at crossing points, they are divided into two types, i.e., the differentiable type and the nondifferentiable type. As for the differentiable type, two models have been proposed for Buck converters under voltage-mode control (single-loop control) and peak current-mode control (dual-loop control) separately [16], [17]. They explain the influences of MWRs by their derivatives at crossing points, which are verified by Taylor-series expansion. Similar to the articles presented in [14] and [15], finite sideband components are adopted in these models. As for the nondifferentiable type, another two models have been proposed for Buck converters under voltage-mode control (single-loop control) and current-mode control (single-loop control), respectively [18], [19]. They claim that influences of MWRs are dependent on their left derivatives at crossing points. However, this conclusion is built on the premise that infinite sideband components have been considered. The physical reason is that they analyze perturbated MWRs from closed-loop view, which makes crossing points locating in the valley of MWRs, as shown in Fig. 2. Infinite sideband components have naturally been included in the perturbated MWRs, which largely complicates these models.

This article aims to propose the accurate and simplified model for Buck converters with nondifferentiable MWRs. Voltage-mode control is chosen for better comparisons with the existing research articles. Contributions can be highlighted as follows. Perturbated MWRs are analyzed from an open-loop view with the aid of a nonsinusoidal small-signal perturbation method, which enables the proposed model to consider finite sideband components merely. Quantitative guidance is proposed to choose dominant sideband components. The stable working region and control design of wide-input high-bandwidth Buck converters are talked about according to the proposed model.

The rest of this article is organized as follows. In Section II, steady-state models for MWRs are built. In Section III, the accurate small-signal model for Buck converters is derived. Section IV introduces the stable working region and control design for wide-input high-bandwidth Buck converters. Section V verifies the proposed model by the simulations and experiments. Finally, Section VI concludes this article.

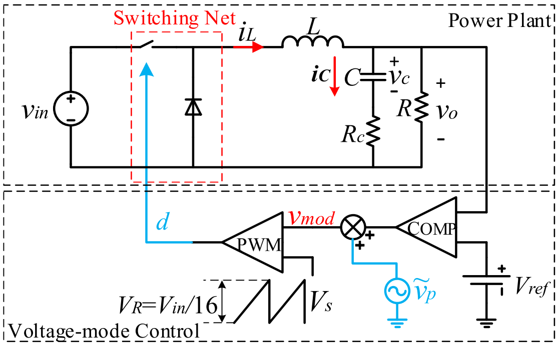

Fig. 3. Wide-input Buck converter under voltage-mode control.

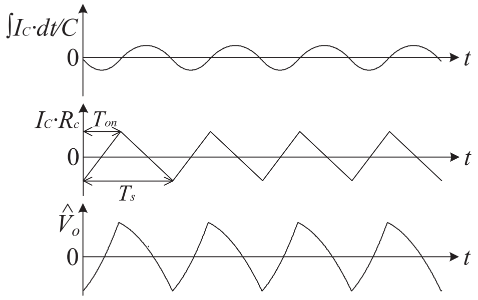

Fig. 4. Waveform of $\hat{V}_o$.

In this article, capital letters indicate quantities in steady state, small letters indicate quantities in the perturbed state, and letters with tildes indicate small-signal perturbations.

II. STEADY-STATE ANALYSES FOR MWRs

The accuracy of small-signal models highly depends on the accuracy of corresponding steady-state models. Steady-state analyses for MWRs are necessary. First, the mechanism of wide-input Buck converters under voltage-mode control is introduced. Then, different types of MWRs are talked about. Finally, steady-state modeling methods for MWRs are summarized.

A. Introduction of Wide-Input Buck Converters Under Voltage-Mode Control

A wide-input Buck converter under voltage-mode control is shown in Fig. 3. The output voltage v_o is fed back to the compensator to create the modulation waveform v_{mod}. It is compared with the sawtooth carrier waveform V_s to obtain the control signal d by the PWM. According to the small-signal averaged model, the loop gain is proportional to the input voltage v_{in} and inversely proportional to the amplitude of V_s, V_R [1]. In practical applications, V_R is proportional to V_{in} for guaranteeing a stable loop gain design when the input voltage changes, which is achieved by control chips [20].

B. Different Types of MWRs

The capacitor current I_C is assumed as the ac component of the inductor current I_L. As shown in Fig. 4, the ripple of V_o ($\hat{V}_o$) is composed of the capacitor integration and the equivalent series

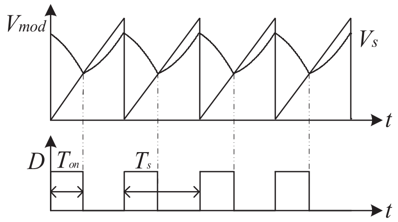

Fig. 5. MWRs with nondifferentiable crossing points.

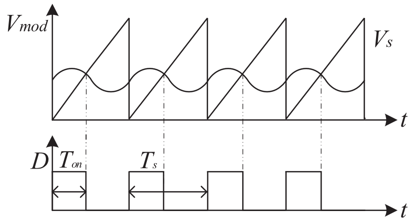

Fig. 6. MWRs with differentiable crossing points.

resistance (ESR) product of I_C, where $T_{\rm on}$ is the steady-state ON-time and T_s is the switching period. $\hat{V}_o$ contains harmonics with integer multiples of the switching frequency f_s.

Proportional (P) and proportional–integral (PI) controllers are equal to all-pass filters, which make MWRs ($\hat{V}_{\rm mod}$) share the same geometry as $\hat{V}_o$. As shown in Fig. 5, $\hat{V}_{\rm mod}$ contains abundant frequency components, which are nondifferentiable at crossing points. External zeros and poles are added into P or PI controllers, such as two zeroes and three poles controllers, to restrain high-frequency noises and compensate phase margin. These controllers work as low-pass filters, which filter out the majority of harmonics above f_s. $\hat{V}_{\rm mod}$ is dominated by the switching frequency harmonic, which is differentiable at crossing points, as shown in Fig. 6.

C. Steady-State Modeling Methods for MWRs

Generalized average model is a multifrequency large-signal model describing state variables by dc values and first-order harmonics [21], [22], which is suitable to model differentiable MWRs dominated by switching frequency component. The detailed modeling process can be found in [16].

As for nondifferentiable MWRs, time-domain analyses are more applicable than frequency-domain analyses due to infinite harmonics. According to Fig. 4, $\hat{V}_o$ can be derived as

$$\hat{V}_o(t) = R_c I_C\left(t\right) + \frac{1}{C}\int_o^t I_C\left(\tau\right) d\tau \tag{1}$$

where I_C is represented as

$$I_C\left(t\right) = \begin{cases} \frac{(1-D)V_{\rm in}}{L}\left(t - nT_s - \frac{1}{2}T_{\rm on}\right) \\ \quad nT_s < t < nT_s + T_{\rm on} \\ \frac{(1+D)V_{\rm in}T_{\rm on}}{2L} - \frac{DV_{\rm in}}{L}\left(t - nT_s\right) \\ \quad nT_s + T_{\rm on} \le t < \left(n+1\right)T_s \end{cases} \tag{2}$$

where D represents the duty ratio in the steady state. Controller effects are equal to a negative proportional coefficient $-k_p$.

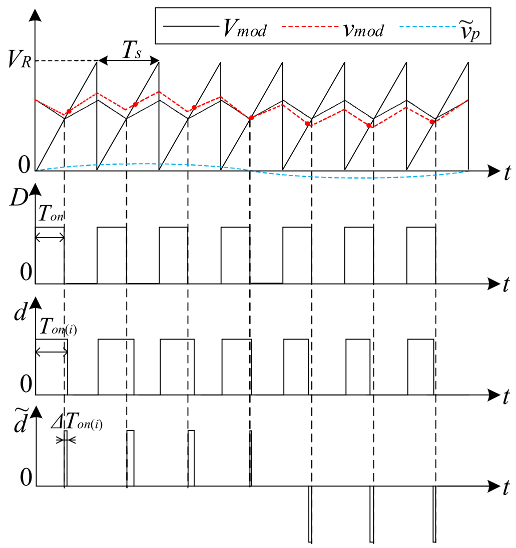

Fig. 7. Working mechanism of PWM under small-signal perturbation.

Finally, $\hat{V}_{\rm mod}$ is obtained as

$$\hat{V}_{\rm mod}\left(t\right) = -k_p\left(R_c I_C\left(t\right) + \frac{1}{C}\int_o^t I_C\left(\tau\right) d\tau\right). \tag{3}$$

III. ACCURATE SMALL-SIGNAL MODEL FOR BUCK CONVERTERS

First, a single-frequency small-signal model considering nondifferentiable MWR is derived for PWM from an open-loop view. Then, it is extended to be a multifrequency small-signal model by considering switch sampling. Finally, quantitative guidance is proposed to choose dominant sideband components.

A. Single-Frequency Small-Signal Model for PWM

Fig. 7 shows the working mechanism of perturbated PWM, where $T_{{\rm on}(i)}$ and $\Delta T_{{\rm on}(i)}$ are the ON-time and ON-time perturbation of the ith switching cycle separately. A single-frequency small-signal model describes a relationship between the single-frequency input perturbation $\tilde{v}_p$ and the same frequency component of the output perturbation $\tilde{d}$. $\tilde{v}_p$ is defined as

$$\tilde{v}_p\left(t\right) = V_p \sin\left(\omega_p t - \theta_p\right) \tag{4}$$

where V_p, ω_p, and θ_p are the amplitude, frequency, and phase angle, respectively.

Here, perturbated MWRs are considered from open-loop view, which means $\tilde{v}_p$ is directly added to steady-state MWRs to form perturbated MWRs. Obviously, crossing points move slightly under the perturbation. When $T_{{\rm on}(i)}$ is smaller than $T_{\rm on}$, they move to the left side of perturbated MWRs; when $T_{{\rm on}(i)}$ is larger than $T_{\rm on}$, they move to the right side of perturbated MWRs. This characteristic is the main difference comparing with analyses in [18] and [19], where crossing points always locate in valleys of perturbated MWRs. Now that both sides of MWRs contribute to the build of the geometric relationship under the perturbation, the left and right derivatives of MWRs at crossing points should be obtained from (3)

$$S_{\text{left}} = \hat{V}'_{\text{mod}}\left(T_{\text{on}-}\right) = -k_p\left(R_c I'_C\left(T_{\text{on}-}\right) + \frac{I_C\left(T_{\text{on}}\right)}{C}\right) \tag{5}$$

$$S_{\text{right}} = \hat{V}'_{\text{mod}}\left(T_{\text{on}+}\right) = -k_p\left(R_c I'_C\left(T_{\text{on}+}\right) + \frac{I_C\left(T_{\text{on}}\right)}{C}\right) \tag{6}$$

where $I'_C(T_{\text{on}-})$, $I'_C(T_{\text{on}+})$, and $I_C(T_{\text{on}})$ are calculated from (2) as

$$I'_C\left(T_{\text{on}-}\right) = \left(1-D\right)V_{\text{in}}/L \tag{7}$$

$$I'_C\left(T_{\text{on}+}\right) = -DV_{\text{in}}/L \tag{8}$$

$$I_C\left(T_{\text{on}}\right) = D\left(1-D\right)V_{\text{in}}T_s/2L. \tag{9}$$

As shown in Fig. 7, the amplitudes of modulation waveforms and carrier waveforms are equal at crossing points under steady state and perturbated state, which can be represented as

$$V_{\text{mod}}\left(t_i + T_{\text{on}}\right) = \frac{V_R}{T_s}T_{\text{on}} \tag{10}$$

$$V_{\text{mod}}\left(t_i + T_{\text{on}(i)}\right) + \tilde{v}_p\left(t_i + T_{\text{on}(i)}\right) = \frac{V_R}{T_s}T_{\text{on}(i)} \tag{11}$$

where t_i represents the beginning of the *i*th switching cycle. By subtracting (10) from (11), perturbated amounts are remained as

$$\tilde{v}_p\left(t_i + T_{\text{on}(i)}\right) = \left(\frac{V_R}{T_s} - S_{m(i)}\right)\Delta T_{\text{on}(i)} \tag{12}$$

where $S_{m(i)}$ represents the left or right derivative based on the following equation:

$$S_{m(i)} = \begin{cases} S_{\text{left}} & \Delta T_{\text{on}(i)} < 0 \\ S_{\text{right}} & \Delta T_{\text{on}(i)} > 0. \end{cases} \tag{13}$$

$S_{m(i)}$ is divided into common-mode and differential-mode parts as

$$S_{mc} = \left(S_{\text{left}} + S_{\text{right}}\right)/2 \tag{14}$$

$$S_{md(i)} = \begin{cases} \left(S_{\text{left}} - S_{\text{right}}\right)/2 & \Delta T_{\text{on}(i)} < 0 \\ -\left(S_{\text{left}} - S_{\text{right}}\right)/2 & \Delta T_{\text{on}(i)} > 0. \end{cases} \tag{15}$$

Therefore, (12) can be reorganized as

$$\tilde{v}_p\left(t_i + T_{\text{on}(i)}\right) = \left(\frac{V_R}{T_s} - S_{mc}\right)\Delta T_{\text{on}(i)} - S_{md(i)}\Delta T_{\text{on}(i)}. \tag{16}$$

A sampling signal of $\tilde{v}_p$ with switching frequency is denoted as

$$\tilde{v}_p^*\left(t\right) = \sum_{i=1}^{+\infty} \tilde{v}_p\left(t\right)\cdot\delta\left[t - \left(t_i + T_{\text{on}}\right)\right]. \tag{17}$$

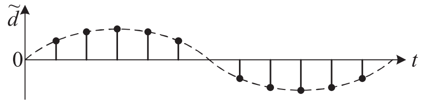

Fig. 8. Sketch map of $\tilde{d}(t)$.

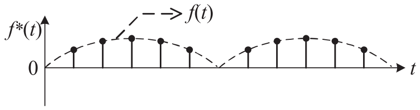

Fig. 9. Sketch map of $f^*(t)$ and $f(t)$.

As shown in Fig. 7, $\tilde{d}$ is the control signal perturbation composed of narrow rectangles, which can be assumed as a series of pulses with heights of $\Delta T_{\text{on}(i)}$ according to area equivalence principle

$$\tilde{d}\left(t\right) = \sum_{i=1}^{+\infty} \Delta T_{\text{on}(i)}\cdot\delta\left[t - \left(t_i + T_{\text{on}}\right)\right]. \tag{18}$$

By substituting (16) and (17) into (18), $\tilde{d}$ is reorganized as

$$\tilde{d}\left(t\right) = \frac{\tilde{v}_p^*\left(t\right) - f^*\left(t\right)}{V_R/T_s - S_{mc}} \tag{19}$$

where $f^*(t)$ is defined as

$$\begin{aligned} f^*\left(t\right) &= \sum_{i=1}^{+\infty} S_{md(i)}\Delta T_{\text{on}(i)}\cdot\delta\left[t - \left(t_i + T_{\text{on}}\right)\right] \\ &= -\frac{S_{\text{left}} - S_{\text{right}}}{2}\left|\tilde{d}\left(t\right)\right|. \end{aligned} \tag{20}$$

Equation (19) is further transferred to *s* domain as

$$\tilde{d}\left(s\right) = \frac{\tilde{v}_p^*\left(s\right) + f^*\left(s\right)}{V_R/T_s - S_{mc}}. \tag{21}$$

The existence of $f^*(s)$ is a barrier to derive $\tilde{d}(\omega_p)$ from (21). Therefore, a nonsinusoidal small-signal perturbation denoted as (22) is utilized to solve this issue

$$\tilde{v}_{pn}\left(t\right) = \tilde{v}_p\left(t\right) - f\left(t\right) \tag{22}$$

where $f(t)$ is the envelope of $f^*(t)$. Equation (21) should be reorganized as

$$\tilde{d}\left(s\right) = \frac{\tilde{v}_{pn}^*\left(s\right) + f^*\left(s\right)}{V_R/T_s - S_{mc}} = \frac{\tilde{v}_p^*\left(s\right)}{V_R/T_s - S_{mc}}. \tag{23}$$

According to (23), $\tilde{d}(t)$ can be viewed as a sampling of a sinusoidal signal, as shown in Fig. 8. Based on the sampling theory, $\tilde{d}(\omega_p)$ can be derived as

$$\tilde{d}\left(\omega_p\right) = \frac{\tilde{v}_p^*\left(\omega_p\right)}{V_R/T_s - S_{mc}} = \frac{\tilde{v}_p\left(\omega_p\right)/T_s}{V_R/T_s - S_{mc}}. \tag{24}$$

Based on (20), $f^*(t)$ is proportional to the absolute value of $\tilde{d}(t)$, which means $f(t)$ is a periodic signal with a frequency of $2\omega_p$, as shown in Fig. 9. Harmonics of $f(t)$ are located at integer times of $2\omega_p$, which indicates $f(\omega_p)$ is 0. According to (22),

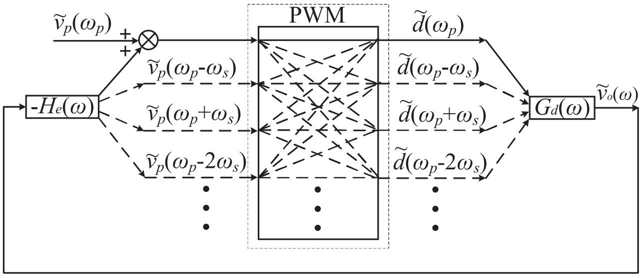

Fig. 10. Multifrequency small-signal model of Buck converters.

$\tilde{v}_{pn}(\omega_p)$ can be derived as

$$\tilde{v}_{pn}\left(\omega_p\right)=\tilde{v}_p\left(\omega_p\right)-f\left(\omega_p\right)=\tilde{v}_p\left(\omega_p\right). \tag{25}$$

Finally, the single-frequency small-signal model for PWM is obtained as

$$\frac{\tilde{d}\left(\omega_p\right)}{\tilde{v}_{pn}\left(\omega_p\right)}=\frac{\tilde{d}\left(\omega_p\right)}{\tilde{v}_p\left(\omega_p\right)}=\frac{1}{V_R-S_{mc}T_s}. \tag{26}$$

According to (26), the influences of nondifferentiable MWRs can be equivalent to the average of left and right derivatives at crossing points, i.e., S_{mc}.

B. Multifrequency Small-Signal Model for Buck Converters

Both the power plant and PI controller, as shown in Fig. 3, are linear parts, and their transfer functions are derived as follows:

$$G_d\left(\omega\right)=V_{\text{in}}\frac{1+j\omega R_cC}{-LC\omega^2+j\omega\left(\frac{L}{R}+R_cC\right)+1} \tag{27}$$

$$H_e\left(\omega\right)=k_p+\frac{k_i}{j\omega}. \tag{28}$$

According to (23), $\tilde{d}$ contains abundant harmonics, i.e., $\tilde{d}(\omega_p)$, $\tilde{d}(\omega_p\pm\omega_s)$, $\tilde{d}(\omega_p\pm 2\omega_s)$, $\tilde{d}(\omega_p\pm 3\omega_s)$, etc. These harmonics flow through the feedback loop to perturbate PWM again. By combining this multifrequency characteristic of PWM with other linear parts, the system model can be obtained, as shown in Fig. 10.

Relationships between the input and output harmonics of PWM can be obtained from (29) based on Sampling Theory

$$\frac{\tilde{d}\left(\omega+i\omega_s\right)}{\tilde{v}_p\left(\omega\right)}=\frac{e^{-j2iD\pi}}{V_R-S_{mc}T_s}i\in Z. \tag{29}$$

$T_S(\omega_p)$ represents the loop gain predicted by the single-frequency small-signal model (only considering the solid lines in Fig. 10), as shown in the following equation:

$$T_S\left(\omega_p\right)=\frac{1}{V_R-S_{mc}T_s}G_d\left(\omega_p\right)H_e\left(\omega_p\right). \tag{30}$$

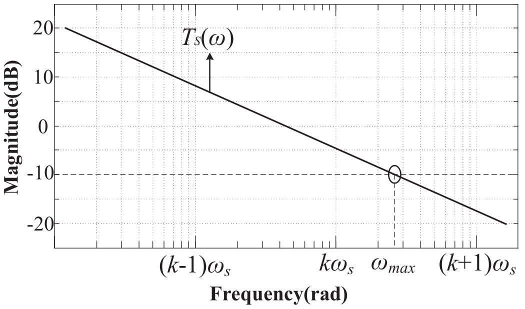

Fig. 11. Quantitative choice of *k*.

The predicted loop gain by the proposed model can be derived as follows, with the aid of the matrix-based method [15]:

$$T_G\left(\omega_p\right)=\frac{T_S\left(\omega_p\right)}{1+\sum\limits_{\substack{i=-(k+1)\\ i\neq 0}}^{k}T_S\left(\omega_p+i\omega_s\right)}\quad 0<\omega_p<\omega_s. \tag{31}$$

$T_S(\omega_p+i\omega_s)$ in the denominator of (31) is corresponding to the selected sideband component one by one. How to decide the nonnegative integer *k* will be introduced in the next part.

C. Quantitative Choice of Dominant Sideband Components

Different choices of dominant sideband components are utilized in different research articles about multifrequency models [14]–[17], [23]. However, all of them are qualitative methods lacking engineering guidance. A quantitative choice strategy is proposed to cover this shortage.

According to (30), $T_S(\omega)$ features a low-pass characteristic by containing the product of power plant and control transfer functions, which means low frequency $T_S(\omega_p+i\omega_s)$ is more considerable in (31). When $\omega_p\in(0,\ 0.5\omega_s)$, $|\omega_p-(i+1)\omega_s|$ is larger than $|\omega_p+i\omega_s|$; when $\omega_p\in(0.5\omega_s,\ \omega_s)$, $|\omega_p-(i+1)\omega_s|$ is smaller than $|\omega_p+i\omega_s|$. Therefore, $T_S[\omega_p-(i+1)\omega_s]$ and $T_S[\omega_p+i\omega_s]$ are considered together for $\omega_p\in(0,\ \omega_s)$, as shown in (31).

As shown in Fig. 11, $T_S(\omega_p+k\omega_s)$ and $T_S[\omega_p-(k+1)\omega_s]$ are largely attenuated with the increase of *k*. A quantitative choice strategy is proposed according to experiences: find the maximum solution $\omega_{\max}$ in the frequency domain to make $|T_S\left(\omega\right)|$ equivalent to -10 dB; *k* is defined as round($\omega_{\max}/\omega_s$). Other sideband components are ignored due to limited influences on the model's accuracy. This strategy can be applied for multifrequency models under different application sceneries.

IV. STABLE WORKING REGION AND CONTROL DESIGN FOR WIDE-INPUT HIGH-BANDWIDTH BUCK CONVERTERS

Based on Sections II and III, $\hat{V}_{\text{mod}}$ has significant influences on the steady-state and small-signal models. This section talks about the stable working region and control design of wide-input high-bandwidth Buck converters from these two aspects.

TABLE I
PARAMETERS OF WIDE-INPUT BUCK CONVERTER

Parameter	Value	Parameter	Value
L/μH	6.5	V_o/V	5
C/μF	7.5	f_s/kHz	300
R_c/Ω	0.11	V_R/V	V_{in}/16
R/Ω	1	k_p	1.5
V_{in}/V	5.6~50	k_i	1.5×10^4

A. Parameters of Power Plant and Control

System parameters are given in Table I for further analyses. PI parameters with high-bandwidth design are utilized to outstand influences caused by $\hat{V}_{\text{mod}}$; the wide-input region of V_{in} is limited between 5.6–50 V to satisfy the standards of duty-ratio constraints in practical applications.

B. How to Find Stable Working Region

As shown in Fig. 5, the right-side MWRs of crossing points are possible to intersect again with carrier waveforms to threat the system stability. When $\hat{V}_o$ is dominated by capacitor voltage ripple, the right-side derivative of MWRs is commonly smaller than the slope of carrier waveforms and the system stability can be guaranteed. While the stable working region is possible to be limited when $\hat{V}_o$ is dominated by ESR voltage ripple. Under this situation, the derivative contributed by ESR remains constant and plays the main role of the MWR derivative. Therefore, the right-side MWR derivative can be assumed as

$$S_{\text{right\_approx}} = \frac{k_p R_c D V_{\text{in}}}{L}. \tag{32}$$

The slope of the carrier waveform can be obtained by Table I

$$S_e = V_R f_s = V_{\text{in}} f_s / 16. \tag{33}$$

A conservative boundary is proposed in (34) to make sure enough stability margin for the system

$$S_{\text{right\_approx}} < \frac{3}{4} S_e. \tag{34}$$

Then, the boundary for the duty ratio is obtained from (34) as

$$D \leq \frac{3 f_s L}{64 k_p R_c}. \tag{35}$$

According to (35), R_c has a big influence on the stable working region, which shows the importance of capacitor selections. The three most widely used capacitor types in switching power supplies are electrolytic capacitor, ceramic capacitor, and tantalum capacitor. Generally, electrolytic capacitors have large ESRs; ceramic capacitors have small ESRs; tantalum capacitors are in the middle of them [24]. However, different voltage levels and manufacturing qualities also influence ESRs.

If large-ESR capacitors are utilized under P or PI control, nondifferential MWRs are outstanding to increase the risk of the second crossing. A smaller R_c corresponds to a larger stable working region. For parameters, as given in Table I, the stable working region is $0.1 \leq D \leq 0.55$.

Another stability judgment is from the small-signal model. A correction factor $K(D)$ is defined to reflect influences of MWRs on loop gains as follows:

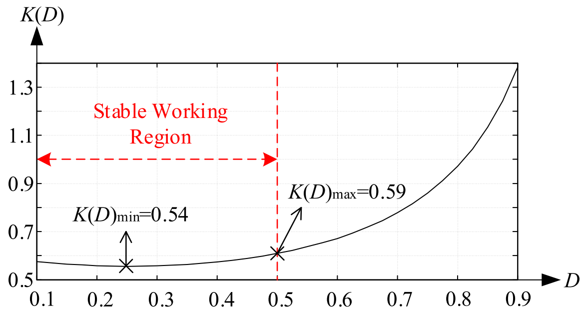

Fig. 12. Functional graphs of $K(D)$.

$$\begin{aligned} K(D) &= \frac{V_R}{V_R - S_{mc} T_s} \\ &= \frac{1}{1 + \frac{16 k_p T_s [R_c C (1-2D) + T_s D (1-D)]}{2LC}}. \end{aligned} \tag{36}$$

Then, (31) can be reorganized as

$$T_G(\omega_p) = \frac{K(D) \cdot T_{\text{av}}(\omega_p)}{1 + K(D) \cdot \sum\limits_{\substack{i=-(k+1) \\ i \neq 0}}^{k} T_{\text{av}}(\omega_p + i\omega_s)} \tag{37}$$

where $T_{\text{av}}(\omega_p)$ represents the loop gain derived by the averaged small-signal model, as shown in (38), which remains the same under different conditions of MWRs

$$T_{\text{av}}(\omega_p) = G_d(\omega_p) H_e(\omega_p) / V_R. \tag{38}$$

According to (37), the bandwidth increases, and the phase margin reduces with a larger $K(D)$. By solving (37) with the phase margin limitation, the largest $K(D)$, $K(D)_{\text{max}}$, can be derived. Then, any $K(D)$ below $K(D)_{\text{max}}$ belongs to the stable working region.

Here, the phase margin limitation is defined as 25°, and the corresponding $K(D)_{\text{max}}$ is 0.59. The stable working region is described in Fig. 12, which is $0.1 \leq D \leq 0.5$. It is different from the stable working region derived by the steady-state model, which is $0.1 \leq D \leq 0.55$. The final result depends on the intersection of them, which is $0.1 \leq D \leq 0.5$.

C. How to Design Control Parameters

Fig. 13 shows how to obtain a stable high-bandwidth design for the required wide-input range when power plant parameters have been decided.

1) Step one: To reach high bandwidth, k_p should be as large as possible. Based on (35), the maximum of k_p is limited by the maximum duty ratio D_{max}. Therefore, k_p is calculated as follows:

$$k_p = \frac{3 f_s L}{64 R_c D_{\text{max}}}. \tag{39}$$

2) Step two: Choose k_i according to the small-signal averaged model in (38). Place the zero of PI controller suitably.
3) Step three: Calculate $K(D)_{\text{max}}$ and the minimum phase margin of the whole working region based on (36) and (37), respectively.

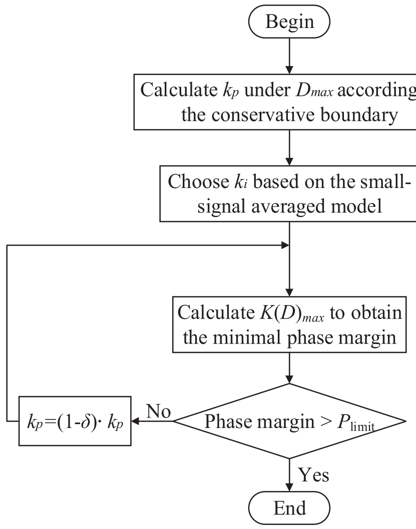

Fig. 13. Control design procedure for wide-input high-bandwidth Buck converters.

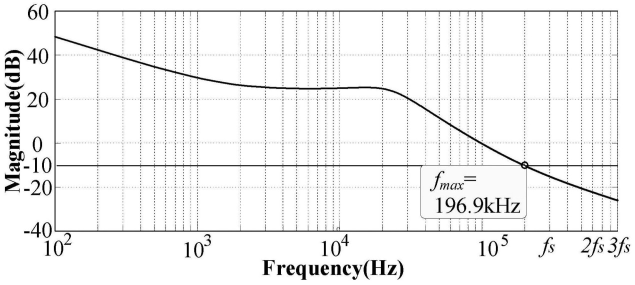

Fig. 14. Bode plots of $T_S(\omega_p)$ when $V_{\text{in}} = 8$ V.

4) Step four: When the minimum phase margin is smaller than the limitation P_{limit}, k_p is reduced by $(1-\delta)$ times to increase the phase margin, where δ represents a small positive amount. Then, go back to Step three until the minimum phase margin satisfies the limitation.

V. VERIFICATIONS

A. Simulated Verifications for Accuracy of the Proposed Model

The system, as shown in Fig. 3, is built in the SIMPLIS software, which performs small-signal ac analysis by a similar scheme in real measurements. Parameters are given in Table I. The specific working condition is $V_{\text{in}} = 8$ V. $T_S(\omega_p)$ is obtained from (30), as shown in Fig. 14, where $f_{\max}$ is 196.9 kHz. Therefore, k equals round($f_{\max}/f_s$) = 1. S_{left} and S_{mc} are derived as -1.72×10^5 and -0.71×10^5 separately from (5) and (14).

In this article, S_{mc} is used to reflect the influences of MWRs. While in [18] and [19], S_{left} takes the place; in [15], 0 takes the place. To show the necessity of considering MWRs and the accuracy of the proposed model, three loop gains predicted by them, i.e., adopting S_{mc}, S_{left}, and 0, are compared with the simulated result, as shown in Fig. 15. In this case, the choice of sideband components is the same as in [15]. As shown in Fig. 15, the matrix-based small-signal model in [15] neglecting influences of MWRs is obviously inaccurate; the model adopting S_{left} does not improve the accuracy and even has larger errors than the model without considering MWRs, which indicates that the model in [18] and [19] is invalid with finite sideband components. The prediction from the proposed model matches the simulated result much better. The tiny discrepancy between them is caused by ignorance of other sideband components. Although the accuracy can be enhanced by increasing k, a balance between the accuracy and simplification is necessary for a successful model. The value of $k = 1$ is valid enough for the stability judgment and control design. The predicted phase margin is 19°, which indicates that the system is easy to be unstable under perturbations.

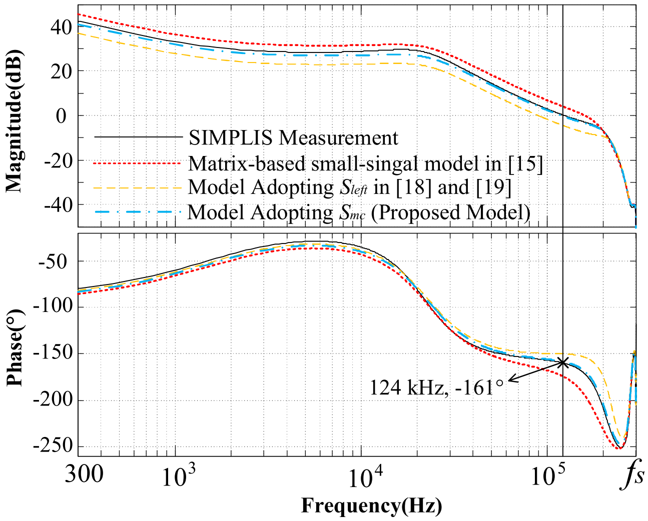

Fig. 15. Bode plots of loop gain obtained by simulation measurement and three small-signal models under $k = 1$.

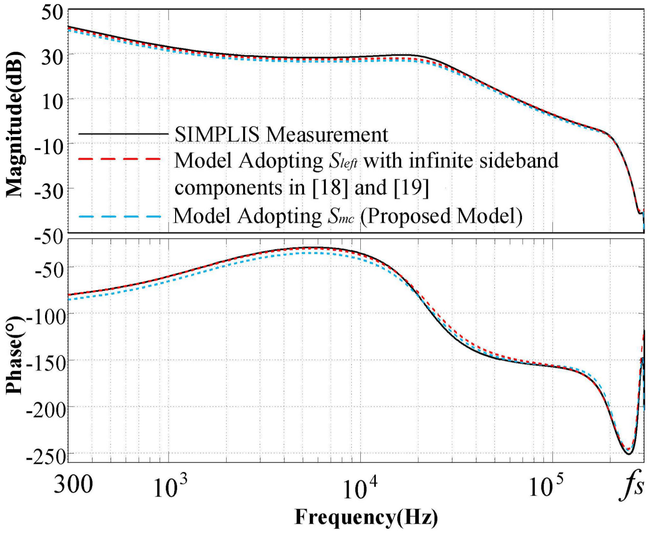

Fig. 16. Bode plots of loop gain obtained by simulation measurement and two small-signal models.

The model in [18] and [19] analyzes MWRs from a closed-loop view, while the proposed model is from an open-loop view. Fig. 16 makes a direct comparison between them. In this case,

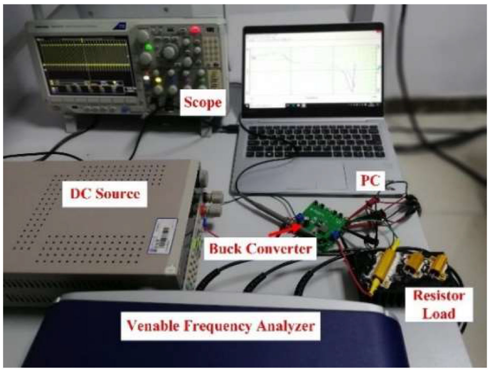

Fig. 17. Schematic diagram of the experimental platform.

infinite sideband components are considered for the model in [18] and [19], while the proposed model is still under $k = 1$. The model in [18] and [19] can be a little more accurate than the proposed model by incorporating infinite sideband components. However, infinite terms also make a big barrier to obtain an analytical solution. Fortunately, this solution can be derived owing to the simple structure of voltage-mode control, but the process is very complex and time consuming [18]. Additionally, it is difficult to be extended to other advanced control strategies. As for the proposed model, it reaches a good balance between accuracy and simplification, which is convenient to be applied to other control strategies, such as peak current-mode control and constant ON-time control.

B. Experimental Verifications for Stable Working Region

An experimental platform is built, as shown in Fig. 17, with the parameters in Table I. Based on the analyses in Section IV-B, the stable working region for the system is $0.1 \leq D \leq 0.5$ and $K(D)_{\max}$ is 0.59 when $V_{\text{in}} = 10$ V$(D = 0.5)$. By substituting $K(D)_{\max}$ into (37), the corresponding largest bandwidth and smallest phase margin are derived as 105 kHz and 26°. The Venable Frequency Analyzer is used to measure the system loop gain under this working condition. As shown in Fig. 18, the measured bandwidth is 112 kHz and the measured phase margin is 18°, which matches well with the theoretical predictions. Deviations between them are mainly due to parameter variations and measurement errors in the real system.

The waveforms under three different working conditions are measured by an oscilloscope, as shown in Fig. 19. Among them, $V_{\text{in}} = 20$ V$(D = 0.25)$ and $V_{\text{in}} = 10$ V$(D = 0.5)$ are within the predicted stable working region and the corresponding waveforms are all stable. When $V_{\text{in}} = 20$ V, the estimated $S_{\text{right\_approx}}$ from Fig. 19(a) is around 1.6×10^5, far smaller than the $S_e(3.75\times10^5)$; when $V_{\text{in}} = 10$ V, the estimated $S_{\text{right\_approx}}$ from Fig. 19(b) is around 0.84×10^5, far smaller than the $S_e(1.875\times10^5)$. They have enough stable margins.

$V_{\text{in}} = 8$ V $(D = 0.625)$ is outside the predicted stable working region. The predicted phase margin by the proposed model is 19°, which is smaller than the phase margin limitation 25°; the estimated $S_{\text{right\_approx}}$ by (32) is 1.27×10^5, which is very close to the $S_e(1.5\times10^5)$. Under this working condition, the system is sensitive to perturbations and easy to be unstable due to limited stability phase margin, as shown in Fig. 19(c).

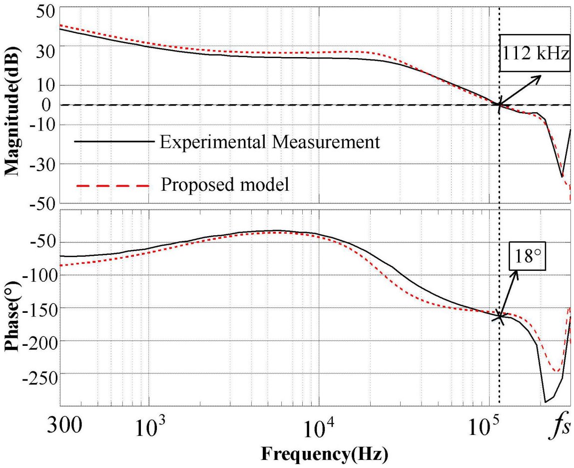

Fig. 18. Bode plots of loop gain obtained by experiments and the proposed model when $V_{\text{in}} = 10$ V.

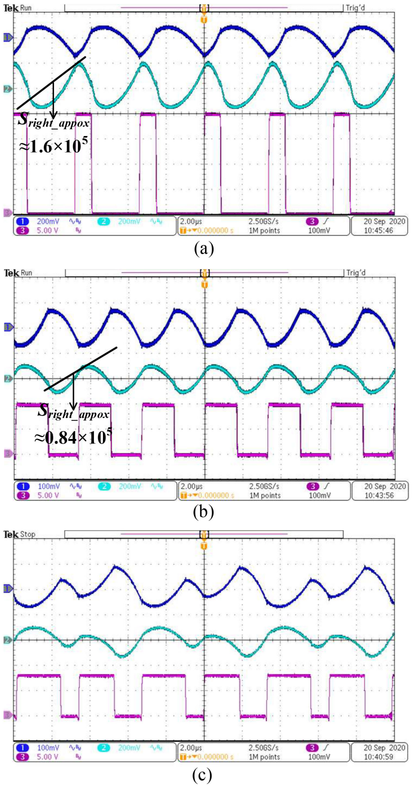

Fig. 19. Experimental waveforms under different input voltages: CH 1, $\hat{V}_o$; CH 2, $\hat{V}_{\text{mod}}$; CH 3, $V_{\text{in}} \times d(t)$. (a) $V_{\text{in}} = 20$ V. (b) $V_{\text{in}} = 10$ V. (c) $V_{\text{in}} = 8$ V.

C. Design Control Parameters for Wide-Input Range

To extend the wide-input range from $0.1 \leq D \leq 0.5$ to $0.1 \leq D \leq 0.9$, control parameters should be designed according to Fig. 13. First, k_p is derived as 0.92 based on (39) under $D_{\max}$

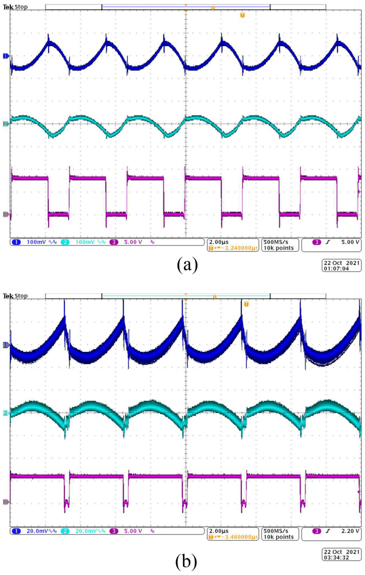

Fig. 20. Experimental waveforms under different input voltages under $k_p = 0.745$: CH 1, $\hat{V}_o$; CH 2, $\hat{V}_{\mathrm{mod}}$; CH 3, $V_{\mathrm{in}} \times d(t)$. (a) $V_{\mathrm{in}} = 8$ V under $k_p = 0.745$. (b) V_{in}=5.6 V under $k_p = 0.745$.

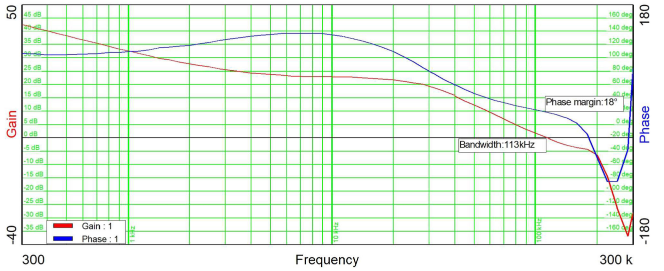

Fig. 21. Bode plots of experimental loop gain when $V_{\mathrm{in}} = 5.6$ V under $k_p = 0.745$.

$= 0.9$. Second, k_i is chosen as 1.5×10^4 based on (38), and the predicted loop gain and phase margin are 93.6 kHz and 40° by the small-signal averaged model. Third, $K(D)_{\max}$ is calculated as 1.221 when D is 0.9 based on (36); the minimum phase margin is obtained as 17.7° by substituting $K(D)_{\max}$ into (37). Fourth, k_p is reduced by $(1-\delta)$ times to increase the phase margin because 17.7° is smaller than $P_{\mathrm{limit}} = 25°$, where δ is chosen as 0.1 here; then go back to the third step until the minimum phase margin satisfies the limitation. After two cycles, k_p is reduced to 0.745 to obtain a suitable minimal phase margin 26° when D is 0.9.

By applying this control design in the experiment, the system works stably during $0.1 \leq D \leq 0.9$. The waveforms under two different working conditions are measured by an oscilloscope, as shown in Fig. 20. The system is stable under $V_{\mathrm{in}} = 8$ V ($D = 0.625$), which is unstable in the original control design as shown in the last part. And the system is also stable under $V_{\mathrm{in}} = 5.6$ V ($D = 0.9$), which is the working condition with a minimum phase margin. As shown in Fig. 21, the measured phase margin is 18° under $V_{\mathrm{in}} = 5.6$ V ($D = 0.9$), which is a little smaller than the theoretical prediction. Real systems are impossible to match models totally; that is why, enough stable margin is necessary for control design.

VI. CONCLUSION

This article proposes the accurate small-signal model for Buck converters under voltage-mode control with nondifferentiable MWRs. It points out that different controller designs are the fundamental reason for causing different types of MWRs, i.e., the differentiable type and the nondifferentiable type, and summarize the steady-state models for each type. Then, the accurate small-signal model for systems with nondifferentiable MWRs is mainly researched, which reveals that the influences can be equivalent to the average of left and right derivatives of MWRs at crossing points. Quantitative guidance with a boundary of -10 dB is used to choose dominant sideband components. Based on the proposed model, the stable working region and control design for wide-input high-bandwidth Buck converters is talked from two dimensions, i.e., steady-state and small-signal models. All these conclusions have been verified with the simulations and experiments.

Further research is going to extend this model to other dc/dc converters under different linear control strategies.

REFERENCES

[1] S. Cuk, “Modelling, analysis, and design of switching converters,” Ph.D. dissertation, Dept. Eng. Appl. Sci., California Inst. Technol., Pasadena, CA, USA, Nov. 1976.

[2] X. Cheng, J. Liu, Zeng Liu, D. Xue, and Z. Liu, “An enhanced multi-frequency small-signal model for the close-loop design in buck converters,” in *Proc. IEEE Energy Convers. Congr. Expo.*, 2018, pp. 1453–1458.

[3] Y. Qiu, K. Yao, Y. Meng, M. Xu, F. C. Lee, and M. Ye, “Control-loop bandwidth limitations for multiphase interleaving buck converters,” in *Proc. 19th Annu. IEEE Appl. Power Electron. Conf. Expo.*, Anaheim, CA, USA, 2004, pp. 1322–1328.

[4] A. Borrell, M. Castilla, J. Miret, J. Matas, and L. García de Vicuña, “Control design for multiphase synchronous buck converters based on exact constant resistive output impedance,” *IEEE Trans. Ind. Electron.*, vol. 60, no. 11, pp. 4920–4929, Nov. 2013.

[5] Y. Panov and M. M. Jovanovic, “Design considerations for 12-V/1.5-V, 50-A voltage regulator modules,” *IEEE Trans. Power Electron.*, vol. 16, no. 6, pp. 776–783, Nov. 2001.

[6] R. Guo, Z. Liang, and A. Q. Huang, “A family of multimodes charge pump based dc–dc converter with high efficiency over wide input and output range,” *IEEE Trans. Power Electron.*, vol. 27, no. 11, pp. 4788–4798, Nov. 2012.

[7] Q. Tong and D. Zhang, “Research on a high output current dc/dc converter with wide input voltage range for space applications,” in *Proc. Int. Conf. Integr. Circuits Microsyst.*, 2016, pp. 205–209.

[8] C.-S. Yeh, X. Zhao, and J.-S. Lai, “A MHz zero voltage switching (ZVS) tapped-inductor buck converter for wide-input high step-down low-power applications,” in *Proc. IEEE 3rd Int. Future Energy Electron. Conf. ECCE Asia*, Kaohsiung, Taiwan, 2017, pp. 494–499.

[9] G. Zhou, M. Leng, Y. Li, Q. Tian, and L. Deng, “A review on modeling of switching converters and their control loops,” *Proc. Chin. Soc. Elect. Eng.*, vol. 40, no. 1, pp. 183–199, Jan. 2020.

[10] P. Maranesi, “Small-signal circuit modeling in the frequency-domain by computer-aided time-domain simulation,” *IEEE Trans. Power Electron.*, vol. 7, no. 1, pp. 83–88, Jan. 1992.

[11] P. G. Maranesi and M. Riva, “Automatic modeling of PWM dc-dc converters,” *IEEE Power Electron. Lett.*, vol. 1, no. 4, pp. 97–100, Dec. 2003.

[12] D. J. Packard, “Discrete modeling and analysis of switching regulators,” Ph.D. dissertation, Dept. Eng. Appl. Sci., California Inst. Technol., Pasadena, CA, USA, 1976.

[13] C.-C. Fang and E. H Abed, “Sampled-data modelling and analysis of the power stage of PWM dc-dc converters,” *Int. J. Electron.*, vol. 88, no. 3, pp. 347–369, 2001.

[14] Y. Qiu, M. Xu, J. Sun, and F. C. Lee, “A generic high-frequency model for the nonlinearities in buck converters,” *IEEE Trans. Power Electron.*, vol. 22, no. 5, pp. 1970–1977, Sep. 2007.

[15] X. Yue, F. Zhuo, S. Yang, Y. Pei, and H. Yi, “A matrix-based multifrequency output impedance model for beat frequency oscillation analysis in distributed power systems,” *IEEE J. Emerg. Sel. Topics Power Electron.*, vol. 4, no. 1, pp. 80–92, Mar. 2016.

[16] X. Cheng, J. Liu, and Z. Liu, “A generalized multifrequency small-signal model for high-bandwidth buck converters under constant-frequency voltage-mode control,” *IEEE Trans. Power Electron.*, vol. 35, no. 8, pp. 8186–8199, Aug. 2020.

[17] X. Cheng, J. Liu, Z. Liu, L. Cheng, and Y. Tu, “An enhanced multifrequency small-signal model for a high-bandwidth PCM buck converter,” in *Proc. IEEE Energy Convers. Congr. Expo.*, 2019, pp. 654–659.

[18] X. Li, X. Ruan, Q. Jin, M. Sha, and C. K. Tse, “Small-signal models with extended frequency range for dc–dc converters with large modulation ripple amplitude,” *IEEE Trans. Power Electron.*, vol. 33, no. 9, pp. 8151–8163, Sep. 2018.

[19] H. T. Mouton, S. M. Cox, B. McGrath, L. Risbo, and B. Putzeys, “Small-signal analysis of naturally-sampled single-edge PWM control loops,” *IEEE Trans. Power Electron.*, vol. 33, no. 1, pp. 51–64, Jan. 2018.

[20] “TPS40170 datasheet,” Texas Instrum., Dallas, TX, USA, 2014. [Online]. Available: https://www.ti.com.cn/cn/lit/ds/symlink/tps40170.pdf

[21] S. R. Sanders, J. M. Noworolski, X. Z. Liu, and G. C. Verghese, “Generalized averaging method for power conversion circuits,” in *Proc. 21st Annu. IEEE Conf. Power Electron. Specialists*, San Antonio, TX, USA, 1990, pp. 333–340.

[22] A. Emadi, “Modeling and analysis of multiconverter dc power electronic systems using the generalized state-space averaging method,” *IEEE Trans. Ind. Electron.*, vol. 51, no. 3, pp. 661–668, Jun. 2004.

[23] S.-F. Hsiao, D. Chen, C.-J. Chen, and H.-S. Nien, “A new multiple-frequency small-signal model for high-bandwidth computer V-core regulator applications,” *IEEE Trans. Power Electron.*, vol. 31, no. 1, pp. 733–742, Jan. 2016.

[24] W.-C. Chen *et al.*, “Reduction of equivalent series inductor effect in delay-ripple reshaped constant on-time control for buck converter with multilayer ceramic capacitors,” *IEEE Trans. Power Electron.*, vol. 28, no. 5, pp. 2366–2376, May 2013.

Xiangpeng Cheng (Student Member, IEEE) received the B.S. degree in electrical engineering and automation in 2016 from Xi’an Jiaotong University, Xi’an, China, where he is currently working toward the Ph.D. degree.

His research interests include small-signal modeling theories for dc/dc converters, impedance modeling of grid-connected converters, stability analyses of multiterminal dc transmission systems, and intelligent optimization algorithm for control design.

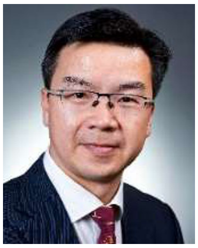

Jinjun Liu (Fellow, IEEE) received the B.S. and Ph.D. degrees in electrical engineering from Xi’an Jiaotong University (XJTU), Xi’an, China, in 1992 and 1997, respectively.

He then joined the XJTU Electrical Engineering School as a Faculty. From late 1999 to early 2002, he was with the Center for Power Electronics Systems, Virginia Polytechnic Institute and State University, Blacksburg, VA, USA, as a Visiting Scholar. In late 2002, he was promoted to a Full Professor and then the Head of the Power Electronics and Renewable Energy Center, XJTU, which now comprises more than 20 faculty members and more than 200 graduate students and carries one of the leading power electronics programs in China. From 2005 to early 2010, he was an Associate Dean of Electrical Engineering School, XJTU, and from 2009 to early 2015, the Dean for Undergraduate Education of XJTU. He is currently an XJTU Distinguished Professor of power electronics. He coauthored three books (including one textbook), authored or coauthored more than 500 technical papers in peer-reviewed journals and conference proceedings, holds 70 invention patents (China/US/EU), and delivered for many times plenary keynote speeches and tutorials at the IEEE conferences or China national conferences. His research interests include modeling, control, and design methods for power converters and electronified power systems, power quality control and utility applications of power electronics, and microgrids for sustainable energy and distributed generation.

Dr. Liu was the recipient of many governmental awards at national level or provincial/ministerial level for scientific research/teaching achievements, the 2006 Delta Scholar Award, the 2014 Chang Jiang Scholar Award, the 2014 Outstanding Sci-Tech Worker of the Nation Award, the 2016 State Council Special Subsidy Award, the IEEE TRANSACTIONS ON POWER ELECTRONICS 2016 and 2021 Prize Paper Awards, and the Nomination Award for the Grand Prize of 2020 Bao Steel Outstanding Teacher Award. He was the IEEE Power Electronics Society Region 10 Liaison and then China Liaison for 10 years, from 2015 to 2019 Executive Vice President, and from 2020 to 2021 Vice President of IEEE PELS. He has been an Associate Editor for the IEEE TRANSACTIONS ON POWER ELECTRONICS since 2006. He was on the Board of China Electrotechnical Society 2012–2020 and was the Vice President in 2013 and the Secretary General in 2018 of the CES Power Electronics Society. He was the Vice President for International Affairs, China Power Supply Society (CPSS), from 2013 to 2021. Since 2013, he has been the Vice Chair of the Chinese National Steering Committee for College Electric Power Engineering Programs. Since 2016, he has been the inaugural Editor-in-Chief for the CPSS TRANSACTIONS ON POWER ELECTRONICS AND APPLICATIONS. He has been the President of CPSS since November 2021.

Zeng Liu (Member, IEEE) received the B.S. degree from Hunan University, Changsha, China, in 2006, and the M.S. and Ph.D. degrees from Xi’an Jiaotong University (XJTU), Xi’an, China, in 2009 and 2013, respectively, all in electrical engineering.

He then joined as a Faculty Member of electrical engineering with XJTU, where he is currently an Associate Professor. From 2015 to 2017, he was with the Center for Power Electronics Systems, Virginia Polytechnic Institute and State University, Blacksburg, VA, USA, as a Visiting Scholar. His research interests include control and stability of power electronics systems with multiple converters for renewable energy and energy storage applications.

Dr. Liu was the recipient of two Prize Paper Awards in the IEEE TRANSACTIONS ON POWER ELECTRONICS. He is currently an Associate Editor for the *IEEE Open Journal of Power Electronics* and the Editorial Board for the *Energies*. He was a Secretary General for the 2019 IEEE 10th International Symposium on Power Electronics for Distributed Generation Systems and the 2020 4th International Conference on HVdc.